Motion of a spherical capsule in branched tube flow with finite inertia

Z. Wang[1], Y. Sui[1]†, A.-V. Salsac[2], D. Barthès-Biesel[2] and W. Wang[1]

[1]School of Engineering and Materials Science, Queen Mary University of London, London E1 4NS, UK

[2]Laboratoire Biomécanique et Bioingénierie (UMR CNRS 7338), Université de Technologie de Compiègne - Sorbonne Universités, CS 60319, 60203 Compiègne, France

We computationally study the transient motion of an initially spherical capsule flowing through a right-angled tube bifurcation, composed of tubes having the same diameter. The capsule motion and deformation is simulated using a three-dimensional immersed-boundary lattice Boltzmann method. The capsule is modeled as a liquid droplet enclosed by a hyperelastic membrane following the Skalak's law (Skalak *et al.* 1973). The fluids inside and outside the capsule are assumed to have identical viscosity and density. We mainly focus on path selection of the capsule at the bifurcation as a function of the parameters of the problem: the flow split ratio, the background flow Reynolds number Re, the capsule-to-tube size ratio a/R and the capillary number Ca, which compares the viscous fluid force acting on the capsule to the membrane elastic force. For fixed physical properties of the capsule and of the tube flow, the ratio Ca/Re is constant. Two size ratios are considered: $a/R = 0.2$ and 0.4. At low Re, the capsule favors the branch which receives most flow. Inertia significantly affects the background flow in the branched tube. As a consequence, at equal flow split, a capsule tends to flow straight into the main branch as Re is increased. Under significant inertial effects, the capsule can flow into the downstream main tube even when it receives much less flow than the side branch. Increasing Ca promotes cross-stream migration of the capsule towards the side branch. The results are summarized in a phase diagram, showing the critical flow split ratio for which the capsule flows into the side branch as a function of size ratio, Re and Ca/Re. We also provide a simplified model of the path selection of a slightly deformed capsule and explore its limits of validity. We finally discuss the experimental feasibility of the flow system and its applicability to capsule sorting.

Key words: Microcapsules, branched tube, lattice-Boltzmann, immersed boundary, inertia, fluid-structure interactions

1. Introduction

A capsule is a liquid droplet enclosed by a thin membrane which can resist shear deformation. Capsules are widely found in nature in the forms of red blood cells (RBCs), eggs, etc. Artificial capsules have a vast range of applications in food, cosmetic, biomedical and pharmaceutical industries (Bhujbal *et al.* 2014). In many situations, capsules are suspended in a fluid and flow through a complicated network of tubes or channels:

† Email address for correspondence: y.sui@qmul.ac.uk

this is the case for RBCs in the human circulation or for artificial capsules flowing through microfluidic devices. Central to these flows is the dynamic motion of capsules at bifurcations, in particular the question of path selection. A good understanding of this problem is needed to elucidate some intriguing phenomena in human circulation. It will also benefit the design and optimization of microfluidic devices using branched channels, for instance to sort capsules or biological cells depending on their properties.

Extensive in-vivo and in-vitro experiments have been conducted on blood flows in branched capillaries or microchannels (see for instance (Pries *et al.* 1996) or (Popel & Johnson 2005)). It has been well established that the daughter branch with a higher flow rate receives a larger number of RBCs than the other branch; furthermore, one daughter branch can receive no RBC, when its flow rate is very low: it is classically referred to as the Zweifach-Fung effect (Svanes & Zweifach 1968; Fung 1973). Similar phenomena have also been observed in experiments, where the RBCs are modelled as flexible disks and the white blood cells as solid spheres (Chien *et al.* 1985), and in dilute suspensions of solid spheres (Roberts & Olbricht 2006; Doyeux *et al.* 2011). Fenton *et al.* (1985) considered blood flow in a microfabricated branched tube with a diameter of 100 μm for both branches and investigated the effect of cell deformability on the partitioning of RBCs at the bifurcation. Their results, mainly the fractional RBC flux through a side branch as a function of the fractional volumetric flow rate, do not show significant differences between normal and hardened red cells. Two mechanisms have been found to play important roles in the cell enrichment in the high flow rate branch. The first one is the plasma skimming effect due to the particle-free layer near the wall of the vessel (Rong & Carr 1990; Yan *et al.* 1991; Enden & Popel 1994; Carr & Kotha 1995). The second mechanism is the particle screening effect, in which the trajectories of particles deviate from fluid streamlines of the background flow as a result of the hydrodynamic interaction between particles and the vessel geometry at the bifurcation (Wu *et al.* 1992; Doyeux *et al.* 2011). In the dilute limit, the problem has not been thoroughly studied experimentally, possibly due to the difficulty of manipulating individual cells.

Analyzing the motion of one capsule flowing through a branched tube theoretically or numerically is also very challenging due to the strong nonlinear interaction between the elastic capsule, the viscous fluid, and the branched geometry of the tube. The problem has mostly been studied in recent years using two-dimensional numerical models. Secomb *et al.* (2007) pioneered the simulation of flows with capsules through a bifurcation with a finite element model. Using a two-dimensional formulation, they predicted the trajectories of RBCs in branched microvessels of the rat mesentery, which are in qualitative agreement with experimental observations. Later on, the same group found that the cell enrichment in the higher-flow-rate branch is increased by the cell deformability (Barber *et al.* 2008). Recently they studied the effect of cell interaction and found that it leads to a more uniform cell partitioning compared with dilute suspensions, in which cell interaction is negligible (Barber *et al.* 2011). Woolfenden & Blyth (2011) developed a two-dimensional boundary integral method and studied the motion and deformation of a capsule in a channel with a side branch. The capsule was released along the centreline of the parent channel. Their results showed that, at equal flow rate between the two downstream channels, the capsule tends to flow into the side branch in particular when the capsule is highly deformable.

To the best of our knowledge, there is so far no systematic and in-depth three-dimensional numerical study of a deformable capsule in a branched tube. To what extent the results obtained from previous two-dimensional simulations can be applied to three-dimensional flows remains unclear. Almost all the previous studies have considered two-dimensional situations under low-Reynolds-number conditions. The negligible inertia
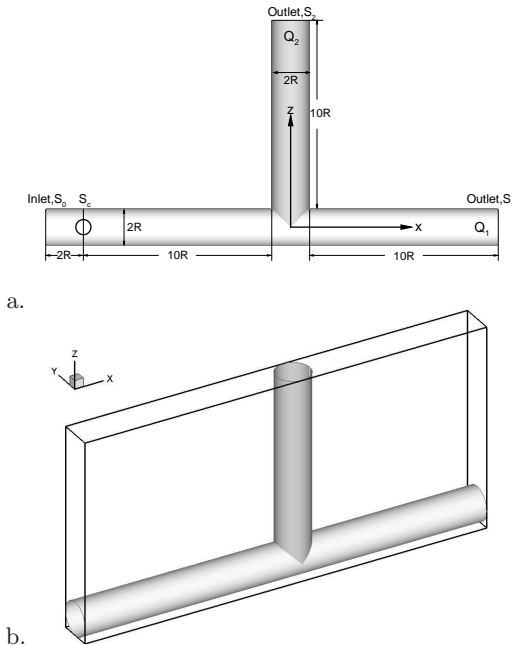
FIGURE 1. (a) Geometry of the branched tube. (b) Geometry of the computational domain.

condition is a good assumption in many biological systems; however, capsules are not necessarily small in size, and the flow speed can be fast in some applications, such as in the case of inertial flow focusing of spherical and anisotropic particles (Di Carlo *et al.* 2007; Masaeli *et al.* 2012). The effect of inertia on path selection of a capsule at a bifurcation remains unknown. In other systems, for example non-spherical particles in shear flows, it has been shown that inertial effect could fundamentally change the dynamics of particles even at low Reynolds number (Rosén *et al.* 2014; Dabade *et al.* 2016). Furthermore, when a capsule approaches the bifurcation, it can sustain high shear stresses, which may damage the capsule membrane. It is therefore meaningful to investigate the membrane tension of the capsule at the bifurcation. In the present study, we address these open questions by means of computational simulations based on an immersed boundary lattice Boltzmann method.

The paper is organized as follows: the problem, governing equations and main parameters are detailed in Section 2; the numerical method and validations are then presented in Section 3. We first present simulation results of flows in a branched tube without a capsule in Section 4. The results for flows with a capsule are presented in Section 5, where we focus on the effects of flow split ratio, flow strength, and capsule properties (i.e. membrane shear elasticity, capsule size) on the capsule path selection. In Section 6, we discuss the main results and compare them to the predictions of a simplified model of the capsule path selection. We also assess the experimental feasibility of the device and discuss its potential for capsules sorting.

2. Problem statement

2.1. *Problem description*

We consider the flow of an initially spherical capsule in a cylindrical tube with a right-angled cylindrical side branch, which has the same diameter $2R$ (Figure 1a). The length of the parent tube is $12R$, and the length of the two daughter tubes is $10R$. A three-dimensional Cartesian coordinate system is defined with the x-axis along the straight tube axis, the z-axis along the side branch axis, and $x = y = z = 0$ at the bifurcation centre. The capsule is initially spherical with diameter $2a$. It is enclosed by a hyperelastic membrane with finite surface shear elasticity and bending stiffness. The fluids inside and outside the capsule have identical viscosity μ and density ρ. Numerical simulations of capsules in a straight tube (Helmy & Barthès-Biesel 1982; Pozrikidis 2005*a,b*) have shown that the capsule migrates to the centreline of the tube and eventually reaches a steady shape. In the present study, the capsule centre is thus initially positioned on the centreline of the parent tube within the cross-section S_c, located at a distance $2R$ from the tube entrance S_0 (Figure 1a).

The fluid motion in the branched tube is governed by the Navier-Stokes equations, which are solved by means of a lattice Boltzmann method (LBM) as detailed in section 3.1. At the tube wall a no-slip boundary condition is imposed. At the upstream inlet S_0 and the two downstream outlets S_1 and S_2, the velocity profiles are set to be the parabolic Poiseuille profiles corresponding to flow rates Q_0, Q_1 and Q_2, respectively, with $Q_0 = Q_1 + Q_2$. The present setup is relevant to microfluidic applications where the flow rate is controlled by multiple syringe pumps.

The thickness of the capsule wall is assumed to be infinitely small. A very thin hyperelastic membrane can be modeled as a zero-thickness elastic surface, with different possible constitutive laws (Barthès-Biesel 2016). Among those, the Skalak's (SK) law (Skalak *et al.* 1973), which was originally proposed to describe the membrane of a RBC, assumes a strain energy function of the form

$$W^{SK} = \frac{1}{4}G_s\left(I_1^2 + 2I_1 - 2I_2\right) + \frac{1}{4}CG_sI_2^2, \tag{2.1}$$

where W is the strain energy density per unit undeformed surface area, G_s is the surface shear elasticity modulus, I_1 and I_2 are the first and second strain invariants of the surface deformation with $I_1 = \lambda_1{}^2 + \lambda_2{}^2 - 2$ and $I_2 = (\lambda_1\lambda_2)^2 - 1 = (dA/dA_0)^2 - 1$. Here dA_0 and dA are the initial and final infinitesimal areas of a membrane element. The terms λ_1 and λ_2 are the principal extension ratios in the plane of the membrane (square root of the eigenvalues of the Cauchy-Green surface deformation tensor). Postulated in such a way, the SK law captures the special feature of biological membranes, which can deform easily under shear while keeping an almost constant surface area. The factor C on the right-hand side of (2.1) must be large to ensure negligible area dilation. The principal membrane tensions τ_1 and τ_2 in the membrane plane are given by

$$\tau_1 = \frac{G_s\lambda_1}{\lambda_2}(\lambda_1^2 - 1 + C\lambda_2^2 I_2), \quad \tau_2 = \frac{G_s\lambda_2}{\lambda_1}(\lambda_2^2 - 1 + C\lambda_1^2 I_2). \tag{2.2}$$

Another constitutive law is the two-dimensional neo-Hookean (NH) law (Green & Adkins 1960), which assumes that the membrane is an infinitely thin sheet of a three-dimensional isotropic volume-incompressible material. The membrane area dilation is compensated by membrane thinning, since the principal extension ratio in the direction perpendicular to the membrane is equal to $\lambda_3 = 1/\lambda_1\lambda_2$. The strain energy function of

the NH law is given by

$$W^{NH} = \frac{1}{2}G_s \left(I_1 - 1 + \frac{1}{I_2 + 1} \right),$$ (2.3)

so that the principal elastic tensions read

$$\tau_1 = \frac{G_s}{\lambda_1 \lambda_2}(\lambda_1^2 - \frac{1}{\lambda_1^2 \lambda_2^2}), \quad \tau_2 = \frac{G_s}{\lambda_1 \lambda_2}(\lambda_2^2 - \frac{1}{\lambda_1^2 \lambda_2^2}).$$ (2.4)

The SK law leads to the same small deformation behavior as the NH law when $C = 1$ (Barthès-Biesel *et al.* 2002). For biological membranes, the factor C is usually much larger than unity, because of their quasi area-incompressibility. In the case of artificial capsules, the SK law has been found to fit experimental data when values of order 1 are used for the factor C (Carin *et al.* 2003; Risso & Carin 2004; Rachik *et al.* 2006). In the present study, the simulations are conducted for capsules enclosed by an SK membrane with $C = 1$, unless otherwise stated.

The bending resistance of the membrane is modelled using Helfrich's formulation (Zhong-Can & Helfrich 1989; Cordasco & Bagchi 2013)

$$E_b = \frac{k_c}{2} \int_A (2H - c_0)^2 dA.$$ (2.5)

In this equation E_b is the bending energy of the capsule membrane, A the surface area, k_c the bending rigidity, H the mean curvature, and c_0 the spontaneous curvature corresponding to the natural state of the unstressed membrane. For the present spherical capsules $c_0 = 0$ has been used.

The interaction between the fluid and capsule membrane is solved by an immersed boundary method (IBM), which is described in section 3.1.

2.2. *Main parameters*

The problem depends on a number of dimensionless parameters, which pertain to the flow configuration and to the capsule properties.

• The branch flow ratio q is the flow rate in the side branch normalized by the flow rate in the parent tube:

$$q = \frac{Q_2}{Q_1 + Q_2},$$ (2.6)

where Q_1 and Q_2 are the flow rates in the downstream main tube and in the side branch, respectively, as indicated in Figure 1a.

• The flow Reynolds number Re is evaluated in the parent tube:

$$Re = \frac{2\rho V R}{\mu},$$ (2.7)

where V is the mean velocity of the Poiseuille flow imposed at the inlet of the parent tube.

• The size ratio a/R compares the size of the capsule to that of the tube.

• The capillary number or dimensionless shear rate Ca measures the ratio between the viscous and elastic forces in the parent tube:

$$Ca = \frac{\mu V}{G_s}.$$ (2.8)

• The dimensionless bending stiffness B measures the relative importance of the

membrane bending to shear elastic effects:

$$B = \frac{k_c}{G_s R^2}. \tag{2.9}$$

Unless otherwise specified, a small value of B has been used ($B = 0.0008$) mainly to prevent the formation of membrane wrinkles (Dupont *et al.* 2015).

Equations (2.7) and (2.8) clearly show that the capillary number and the Reynolds number both increase with V and are related by

$$Ca/Re = \mu^2/2\rho G_s R. \tag{2.10}$$

Their ratio depends only on the physical properties of the tube flow and of the capsule.

3. Numerical method and validation

3.1. *Numerical method*

The present simulations are based on a lattice-Boltzmann method (LBM) to compute the flow coupled with the immersed-boundary method (IBM) of Peskin (1977) for the fluid-capsule interaction. A finite element method is used to obtain the membrane forces. This hybrid method has been validated extensively against results of boundary element simulations and of a small deformation theory for three-dimensional capsules in shear flow (Sui *et al.* 2008*a,b*). The method is only briefly presented here, but more details can be found in the cited references.

The LBM is a kinetic-based approach for simulating fluid flows. Instead of solving the conservation equation of macroscopic properties such as mass or momentum, it consists in modeling the fluid as fictive particles that propagate and collide on a discrete lattice mesh. Solving for the streaming and collision steps leads to solving the following equation (Guo *et al.* 2002*a*):

$$f_i(\mathbf{x} + \mathbf{e}_i \Delta t, t + \Delta t) - f_i(\mathbf{x}, t) = -\frac{1}{\tau}[f_i(\mathbf{x}, t) - f_i^{eq}(\mathbf{x}, t)] + \Delta t F_i, \tag{3.1}$$

where $f_i(\mathbf{x}, t)$ is the distribution function for particles with velocity $\mathbf{e}_i$ at position $\mathbf{x}$ and time t, Δt is the lattice time interval, $f_i^{eq}(\mathbf{x}, t)$ is the equilibrium distribution function, τ is the non-dimensional relaxation time related to the fluid viscosity and F_i is the forcing term. The macroscopic quantities (e.g. velocity, pressure) can be obtained from the particle distribution function. Equation (3.1) is solved on a uniform Cartesian grid in a domain $24R \times 2R \times 12R$ (Figure 1b). Using Chapman-Enskog expansion, the lattice-Boltzmann equation can recover the incompressible Navier-Stokes equations, and therefore the LBM can be considered as an alternative approach for solving the Navier-Stokes equations.

To handle the curved solid wall of the branched tube, we have used the second-order bounce-back scheme developed by Bouzidi *et al.* (2001), which is an accurate and simple treatment. The bounce-back scheme mimics the particle-boundary interaction for no-slip boundary condition by reversing the momentum of the particle colliding with an impenetrable and rigid wall. In the approach of Bouzidi *et al.* (2001), the tube wall can be off the grid points of the regular computational domain (shown in Figure 1b for the present case), which is covered by regular Cartesian mesh. Due to the presence of the wall, the particle distribution functions at the fluid nodes nearest to the wall are unknown in some directions after the streaming step in the LBM: they are reconstructed by a second-order interpolation. The approach has been widely used in treating no-slip

walls with complicated geometries. More details can be found in the paper by Bouzidi *et al.* (2001) and are not repeated here. At the inlet and outlets of the tube, velocity boundary conditions assuming fully developed Poiseuille flows with the appropriate flow rates have been implemented using a second-order non-equilibrium extrapolation method (Guo *et al.* 2002*b*).

In the IBM, a force density is distributed on the Cartesian mesh in the vicinity of the moving boundary in order to account for the presence of the solid boundary. Two different coordinate systems are used: the fluid region is represented by Eulerian coordinates and the membrane of the moving capsule immersed in the fluid by Lagrangian ones. Across the capsule membrane the fluid velocity is continuous and the no-slip boundary condition is satisfied by letting the flexible membrane move at the same velocity as the fluid around it. This motion causes the capsule to deform. There is a jump in fluid stress across the capsule membrane, which is balanced by the membrane stress, calculated from the constitutive laws of the elastic membrane (Equations 2.1, 2.3 or 2.5). The membrane force at a Lagrangian mesh point is distributed on the Eulerian fluid grid points near it by a three-dimensional Dirac delta function. It is commonly accepted that the procedure is efficient if the mesh size ratio between the Lagrangian and Eulerian grids is less than unity. More details can be found in Sui *et al.* (2008*a*).

In the present study, the three-dimensional capsule membrane is discretized into flat triangular elements, following the approach of Ramanujan & Pozrikidis (1998). To discretize the unstressed spherical capsule wall, each triangular face of a regular octahedron is subdivided into 4^n triangular elements. These elements are then projected radially onto the sphere. Note that for a given number of elements, the membrane mesh size depends on the capsule radius. In order to obtain the membrane force due to deformation, a finite element model developed by Charrier *et al.* (1989) and Shrivastava & Tang (1993) has been employed.

3.2. *Validation*

We first validate the model for tube flows by considering a large spherical capsule ($a/R = 0.9$) flowing in a long straight tube (length $20R$). A grid size of $\Delta x = \Delta y = \Delta z = 0.04R$ has been used for the fluid domain. The 3D capsule membrane is discretized into 32,768 flat triangular elements connecting 16,386 nodes, leading to a maximum element edge length $\Delta L_c \sim 0.034R$ and a ratio $\Delta L_c/\Delta x < 0.86$. We obtain the capsule profiles at equilibrium and compare them with those obtained by Hu *et al.* (2012) who used a boundary element method. Very good agreement was achieved in all the cases that were tested. As an illustration, Figure 2 shows the superposition of the deformed profiles obtained with both methods for a capsule with a NH membrane and a size ratio of $a/R = 0.9$ under different capillary numbers. We also conducted simulations with a coarser membrane mesh (8,192 flat triangular elements connecting 4,098 nodes) and found that for $Ca = 0.1$ the deformed profiles were superimposed within graphical precision.

We now turn to the flow of a capsule in the bifurcation and investigate first the influence of the mesh size of the uniform Cartesian grid that is used in the flow domain (Figure 1b). We consider a small capsule ($a/R = 0.4$) with a membrane mesh of 8,192 flat triangular elements connecting 4,098 nodes, leading to $\Delta L_c \sim 0.031R$. Figure 3 shows an example of the influence of the flow grid resolution on the trajectories the capsule in the branched tube for $Re = 0.25$, $Ca = 0.5$ and $q = 0.5$. We find that the trajectories are almost superimposed for all three tested flow grids ($\Delta x = 0.05R, 0.04R$ and $0.031R$). Further refining the membrane mesh to 32,768 flat triangular elements connecting 16,386 nodes
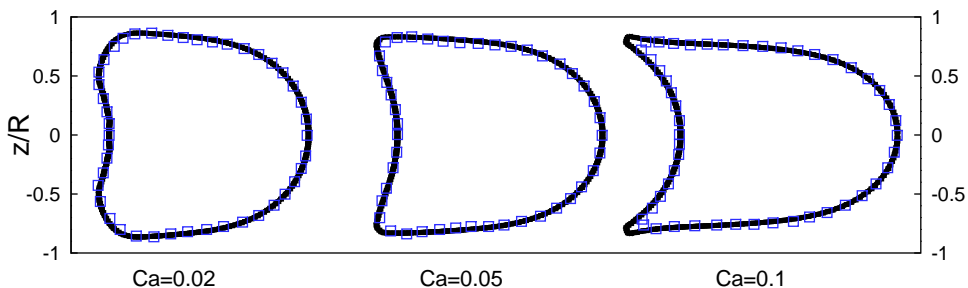
FIGURE 2. Steady profiles of an initially spherical capsule with a NH membrane in a uniform tube flow ($a/R = 0.9$, $Re = 0.125$, $B = 0$) for $Ca = 0.02, 0.05, 0.1$. Black solid lines correspond to the present model with a membrane mesh of 32,768 flat triangular elements connecting 16,386 nodes. The results are compared to the ones obtained by Hu *et al.* (2012) using a boundary element method (square symbols).
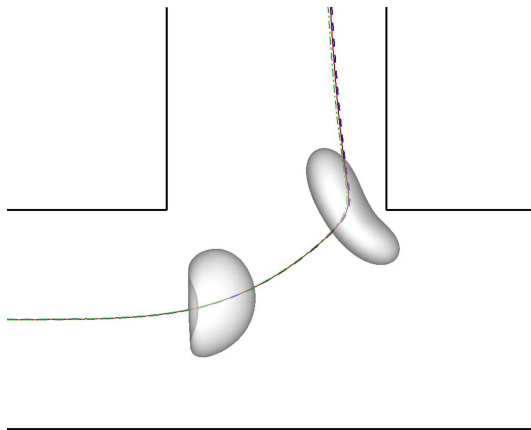

FIGURE 3. Trajectories of a capsule ($a/R = 0.4$) flowing in the branched tube at $Re = 0.25, Ca = 0.5, q = 0.5$. Different grid resolutions are used: $\Delta x = 0.05R$ (dashdot line), $\Delta x = 0.04R$ (solid line), $\Delta x = 0.031R$ (dash line).

($\Delta L_c/\Delta x < 0.38$ for $\Delta x = 0.04R$) does not lead to any visible change in the capsule trajectory. The fluid mesh was chosen, so that the fluid film between the capsule wall and the tube was resolved by at least three grid spaces. Figure 3 illustrates one instance, where the capsule gets very close to the tube wall, as it enters the side branch. We have found that the grid size of $\Delta x = 0.04R$ guarantees, even in this case, that the fluid film contains more than three grid spaces. All the results presented hereafter have thus been obtained for a capsule mesh made of 8,192 flat triangular elements connecting 4,098 nodes and for a fluid grid $\Delta x = 0.04R$.

The effect of the length of the tubes has also been studied. After being released, the capsule deforms into a steady shape, once its centre of mass has travelled a distance of about $5R$ from its initial position in S_c. The $12R$ length of the parent tube is, therefore, long enough for the capsule to reach an equilibrium profile before the bifurcation. We have also examined the effect of the lengths of both downstream tubes by extending them to $14R$, and found almost identical trajectories of the capsule at the bifurcation. Thus the downstream tubes are long enough to exclude the effect of the downstream boundaries

on the capsule motion at the bifurcation. However, it should be noted that the capsule does not reach a steady shape in any downstream branch after passing the bifurcation. Although distance of about $5R$ after the bifurcation is sufficient for the background flow in each branch (i.e. without a capsule) to relax into the fully developed Poiseuille flow at $Re \leqslant 40$, much longer distances are required for the capsule to regain its steady-state shape downstream of the bifurcation. It indeed relies on the capsule migration back towards the tube centreline, which is a very long process (Helmy & Barthès-Biesel 1982; Pozrikidis 2005b; Doddi & Bagchi 2008). As pointed out by Woolfenden & Blyth (2011) and Ye *et al.* (2015), a much longer downstream tube (typically tens of the diameter of the tube) is needed for the capsule to relax into a steady state, which is beyond the scope of the present study.

3.3. *Limitations of the numerical model*

The present simulation has employed the IBM, in which the membrane force is distributed over a band of surrounding Eulerian fluid grids (about $2\Delta x$ on each side of the membrane, according to the Dirac delta function used (Sui *et al.* 2008a)). The second-order approach used to implement the no-slip wall boundary condition in the LBM needs the values of the probability density function at fluid grid points within $2\Delta x$ from the wall. As a result, when the capsule membrane gets close to the wall (i.e. when the thickness of the fluid film between the membrane and the wall is comparable to $2\Delta x$), the present method will not be able to resolve the film flow in the gap. This is likely to happen when a capsule is relatively large ($a/R \geqslant 0.6$) and is close to the bifurcation. However, the film is often thin over a very small area of the capsule membrane only, and therefore the thinness limitation may have a negligible effect on the overall path selection of the whole capsule. This question is left for future investigation and in the present study we only consider small capsules ($a/R \leqslant 0.4$), for which this problem does not occur. It should be noted that in our validation tests presented in Figure 2, the liquid film between the capsule and the tube wall has always been resolved by more than three fluid grids.

4. Flow in the branched tube without a capsule

We consider the flow in the branched tube in absence of any capsule and study the influence of the flow split ratio and Reynolds number. The results will help us analyze some features of capsule dynamics. Furthermore, the results for the background flows will be compared with previous experimental (Rong & Carr 1990; Carr & Kotha 1995) and numerical (Enden & Popel 1992) studies to further validate the present numerical model.

Within each cross-section of the parent tube perpendicular to the tube centreline, one can define a separation line that divides the fluid elements that flow into the side branch from those flowing down the straight tube. We determine the fluid separation line in the cross section S_c and study how it evolves as a function of the flow split ratio and Reynolds number. When a fully developed Poiseuille flow is imposed at the entrance S_0, the flow remains fully developed in cross-section S_c. In order to generate a fluid separation line, 40,000 massless and diffusiveless tracer particles are initially distributed evenly in S_c and released. Their trajectories are calculated using an integration method that is detailed in Sui *et al.* (2012). At the position where a particle is released, a passive scalar ϕ is defined, which takes the value of one when the particle enters the side branch and zero otherwise. The separation line is approximated by the isocontour $\phi = 0.5$. Less than 0.1% of the
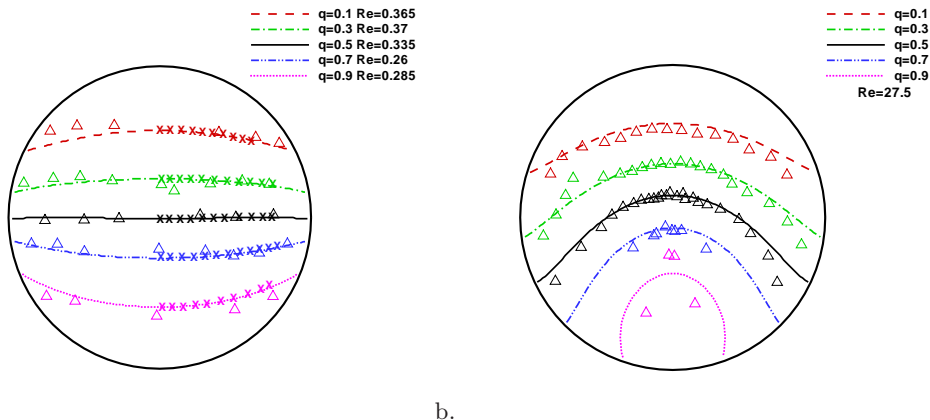
FIGURE 4. Fluid separation lines calculated in cross-section S_c at different Reynolds numbers and branch flow ratios. The cross-section is $2R$ from the entrance, where the flow remains the Poiseuille profile imposed at the inlet. In the cross-section, the fluid elements above the separation line enter the side branch and those below remain in the main tube. (a) Separation lines for flows at low Reynolds numbers. The lines correspond to the present simulation results, the △ symbols to the experimental results of Rong & Carr (1990), the × symbols to the simulation results of Enden & Popel (1992). (b) Separation lines for flows at $Re = 27.5$. The full lines correspond to the present results, the △ symbols to the experiments of Carr & Kotha (1995).
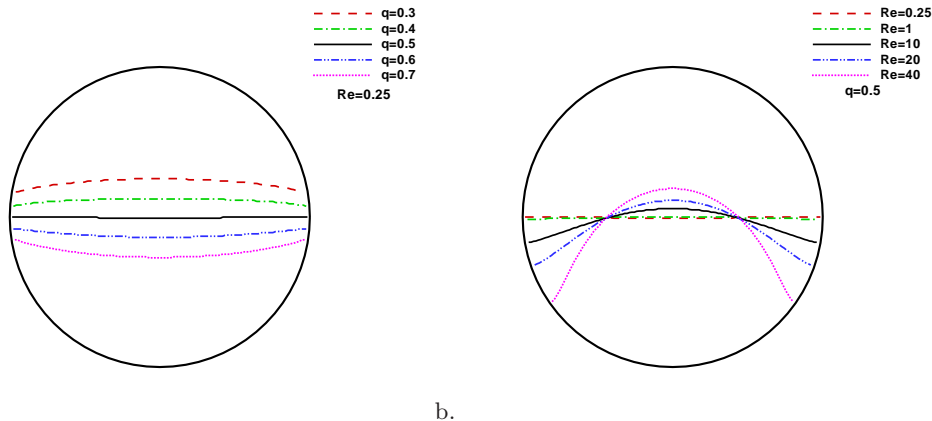

FIGURE 5. Fluid separation lines in branched tube flows. The cross section is the same to that in Figure 4. (a) Separation lines for flows at $Re = 0.25$ with different branch flow ratios; (b) separation lines for flows at different Reynolds numbers with a fixed branch flow ratio $q = 0.5$.

particles are found to get trapped near the apex of the bifurcation, the effect of which can thus be neglected considering the large number of particles released.

The separation lines are shown in Figure 4a for low-Reynolds number ($Re < 1$) flows for different branch flow ratios q. They are compared with the experimental results of Rong & Carr (1990) and with the numerical simulations of Enden & Popel (1992), who considered Stokes flow and used a finite element method. Satisfactory agreements are found in all the cases considered. We can conclude that the flow separation line only depends on the branch flow ratio when $Re < 1$. We also compare the flow separation lines calculated at a higher Reynolds number ($Re = 27.5$) with the experiments of Carr & Kotha (1995) under different flow splits in Figure 4b. Reasonably good agreement is
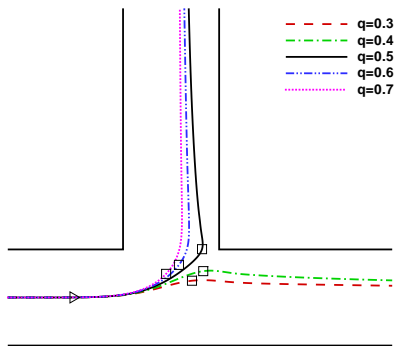
FIGURE 6. Effect of branch flow ratio q on the capsule trajectories ($R = 0.4$, $Re = 0.25$, $Ca = 0.5$). The triangle denotes the position where the bifurcation starts to affect the capsule motion. The squares label the centre of mass positions where the capsule maximum principal tension are the largest (see Figure 9).

again achieved. Note that Re in Carr & Kotha (1995) was defined using the maximum flow velocity.

We can also build the lines for flows at a fixed Reynolds number but different branch flow ratios. The results are presented in Figure 5a for $Re = 0.25$. At equal flow split ($q = 0.5$), the separation line is almost flat and equally divides the cross-sectional area. However, when the branch flow ratio increases (resp. decreases) from 0.5, the separation line moves and bends downwards (resp. upwards).

Figure 5b presents the separation lines for a fixed flow split ratio $q = 0.5$ but different flow Reynolds numbers. When the Reynolds number is increased, the fluid separation line bends towards the side branch. We will later discuss the effect of the geometry of the separation line on the path that the capsule selects.

5. Flow of a capsule in a branched tube

We first present in section 5.1 the 3D flow results for a capsule at small Reynolds number flow, for which inertial effects are negligible. The objective is to set up a reference for the study of the effect of inertia. The effect of Re is then considered in section 5.2, by increasing the flow strength. We show how the tendency of the capsule to flow into the side branch changes with the flow strength, capsule size and membrane elasticity and provide a phase diagram of the capsule path selection in section 5.3.

### 5.1. *Effect of flow split ratio (Re < 1)*

We start from a capsule with a size ratio $a/R = 0.4$ and $Ca = 0.5$ at different branch flow ratios. The Reynolds number based on the parent tube is 0.25. Figure 6 presents the trajectories of the capsule centre of mass for different branch flow ratios. We recover the fact that the capsule favors the branch with the higher flow rate (Barber *et al.* 2008; Woolfenden & Blyth 2011): as the capsule approaches the bifurcation, it slows down, is first attracted by the side branch and flows into it if q is large enough ($q \geqslant 0.5$ in
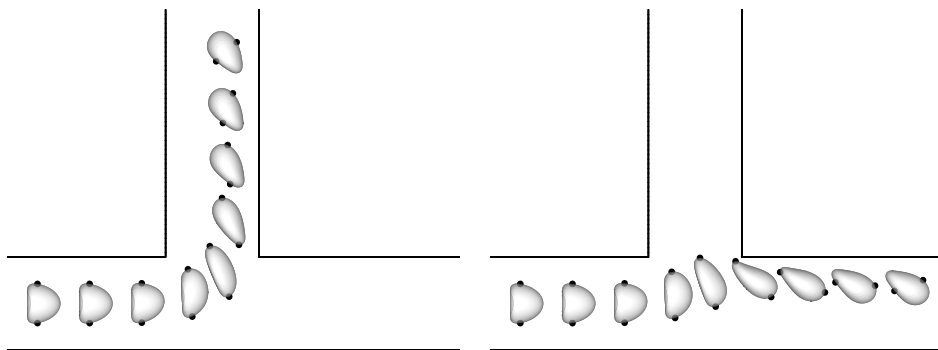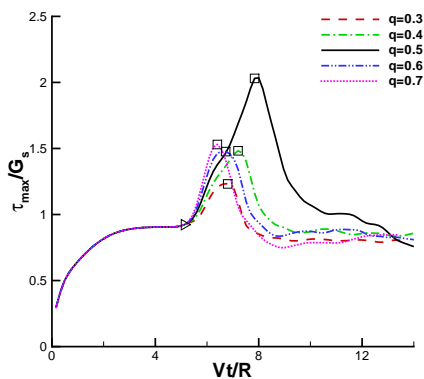
a.   b.

FIGURE 7. Effect of flow split ratio on the path selection of a capsule ($a/R = 0.4$, $Re = 0.25$, $Ca = 0.5$). The profiles are plotted in the xz-plane. The black dots are attached to two material points of the capsule membrane. The profiles are shown at $Vt/R = 4.16, 4.8, 5.44, 6.08, 6.72, 8, 9.28, 10.56, 11.84$. (a) $q = 0.6$, (b) $q = 0.4$.
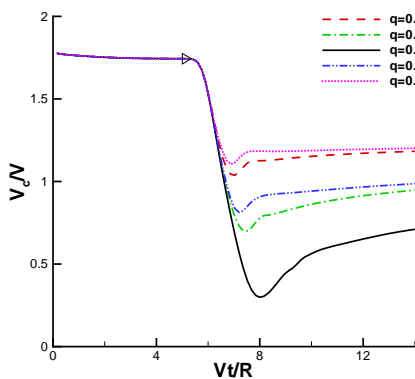
a.   b.

FIGURE 8. Capsule in the branched tube at different branch flow ratios ($a/R = 0.4$, $Re = 0.25$, $Ca = 0.5$). Time evolution of (a) the velocity magnitude V_c/V, and of (b) the maximum principal tension. The squares indicate the dimensionless times when τ_{max} reaches its peak value. The corresponding positions of the capsule centre of mass are shown in Figure 6. The triangle denotes the position where the bifurcation starts to affect the capsule motion.

this case). Otherwise, it migrates back towards the centreline of the straight tube after passing the bifurcation region. In both cases, the capsule does not reach its equilibrium shape when approaching the exit as discussed in section 3.2.

We now investigate the motion and deformation of the capsule near the bifurcation region at different flow splits. Before entering the bifurcation region, the capsule has a parachute shape in the parent tube (Figure 7a,b). The capsule shape starts to deviate from the steady profile when it is about one diameter from the junction (position marked by a triangle in Figure 6). The successive profiles of the capsule in the bifurcation vicinity are shown in Figure 7 for two different flow split ratios ($q = 0.4$ and 0.6). Two membrane material points initially located at the upper and lower sides of the capsule are marked with black dots to facilitate the visualization of the membrane motion. In both cases the capsule first moves upwards towards the side branch, loses its symmetric shape and becomes elongated along the branch flow direction. The capsule enters the side branch
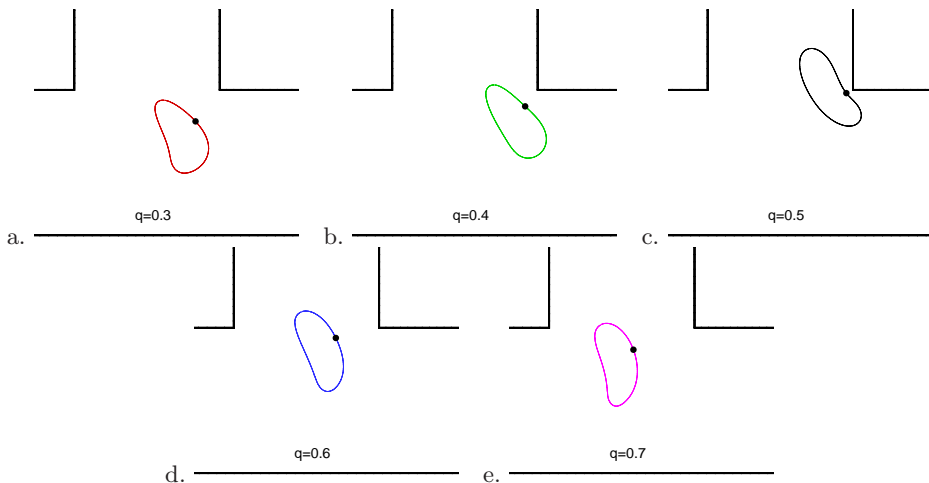
FIGURE 9. Capsule profiles in the xz-plane when the maximum principal tension reaches its peak ($a/R = 0.4$, $Re = 0.25$, $Ca = 0.5$). The black dots show where the principal tension is maximum.

for $q = 0.6$ (Figure 7a), while it remains in the straight tube for $q = 0.4$ (Figure 7b). In both cases, once the capsule has entered either one of the tubes, it is off-centred from the channel axis. It therefore undergoes a clockwise (resp. counterclockwise) tank-treading motion during its migration towards the centreline of the side branch (resp. straight tube), as can be seen from the trajectory of the tracker dots attached to the capsule membrane.

In the parent tube before the bifurcation region, the capsule flows at a steady speed, which is higher than the average speed of the flow (a signature of the Fåhraeus effect (Fåhraeus 1929)). The steady speed of the capsule with $a/R = 0.4$ decreases slightly with the capillary number (not shown), which is consistent with the results of Lefebvre *et al.* (2008) obtained for a capsule in a straight cylindrical channel at confinement ratios $a/R \geqslant 0.8$. When the capsule approaches the bifurcation, it encounters a relatively high pressure: it is thus flattened (as evidenced by the profiles at $Vt/R = 5.44$ and 6.08). Its speed V_c correspondingly decreases to a minimum and then increases back towards a steady value determined by the flow rate in the corresponding downstream tube (Figure 8a).

The maximum principal elastic tension in the membrane $\tau_{max} = \max\,[\tau_1,\,\tau_2]$, where τ_1 and τ_2 are calculated from equation (2.2), is a relevant quantity to evaluate the likelihood of membrane rupture. Figure 8b shows that τ_{max} increases significantly when the capsule approaches the bifurcation. Note that the velocity decrease is almost equal for conditions $q = 0.6$ and 0.4, and for $q = 0.7$ and 0.3. However, for equal flow split ($q = 0.5$), there is a strong decrease in velocity and a large increase in capsule deformation and elastic tension in the membrane. The deformed profiles of the capsules corresponding to the peak of τ_{max} are shown in Figure 9: the initially spherical capsule is significantly deformed. A black dot shows where the peak is reached: the maximum tension occurs where the viscous shear stress exerted by the suspending fluid changes sign.

5.2. *Effect of flow strength and size ratio*

We now turn to the effect of flow strength on the path selection of a capsule for flow regimes where inertia is not negligible. The fluid properties (ρ and μ), the capsule size

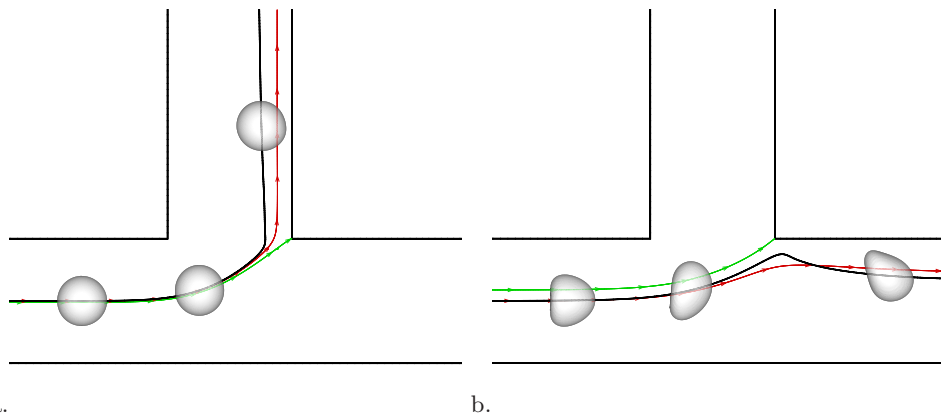a.   b.

FIGURE 10. Effect of flow strength on the capsule trajectory in the symmetric xz-plane ($a/R = 0.4$, $q = 0.52$). (a) $Re = 1$, $Ca = 0.005$; (b) $Re = 40$, $Ca = 0.2$. The thick solid line represents the trajectory of the capsule centre. The dark line with arrows (shown in red online) represents the centre streamline of the undisturbed background flow, while the grey line with arrows (shown in green online) represents the separating streamlines that divides the fluid elements entering the side branch to ones entering the downstream main tube.

($a/R = 0.4$) and the membrane properties (G_s) are fixed. Thus increasing the mean flow speed simultaneously increases the flow Reynolds number and the capillary number. The combined effect of these two parameters is unknown. We first consider the case $Ca = 0.005Re$, for which Ca evolves from a very small value up to 0.2 for the highest flow strength corresponding to $Re = 40$.

The trajectories of the capsule centre of mass and some instantaneous profiles are shown in Figure 10 for two different Reynolds numbers and $q = 0.52$. It is useful to compare the relative positions in the symmetric xz-plane of the capsule centre trajectory, the unperturbed centre streamline (emanating from the centre of S_c in absence of a capsule) and the unperturbed separating streamline (dividing the fluid elements that enter the side branch from those that enter the straight tube). At low mean flow speed ($Re = 1$), the capsule essentially keeps its spherical shape because $Ca = 0.005$ is very small. Its trajectory follows unperturbed centre streamline until it is close to the bifurcation, but deviates from it due to wall exclusion effects inside the side branch. At high flow speed ($Re = 40$), the capillary number is fairly large ($Ca = 0.2$) and the capsule is significantly deformed. Its trajectory first deviates a little from the background streamline moving slightly towards the side branch, but eventually remains in the main tube (like the centre streamline). Therefore increasing the flow speed and thus inertial effect, tends to keep the capsule flowing straight in the main tube. The relative position between the separating streamline and the centre streamline seems to play an important role. Indeed, for $Re = 1$, the separation streamline is initially slightly below the centreline of the parent tube: the centre streamline (and the capsule) thus goes into the side branch. Conversely, for $Re = 40$, the separating streamline is initially above the centreline of the parent tube: the centre streamline (and the capsule) thus goes into the straight tube.

For given values of Re, Ca and q, the capsule trajectory depends on the size ratio a/R. If a capsule has a negligible size and is non-diffusive (i.e., negligible Brownian motion), we expect that it will follow the centre streamline. However, the path selection of a finite size capsule remains an open question. As shown in Figure 11, for $q = 0.56$, a small capsule ($a/R = 0.2$) flows into the straight tube, whereas a large one ($a/R = 0.4$) flows into the side branch. This phenomenon may be partly attributed to the capsule deformation,
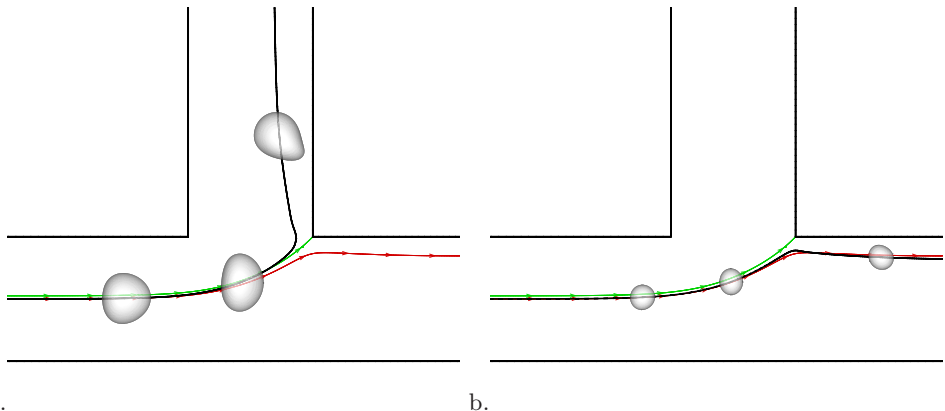
a.   b.

FIGURE 11. Effect of capsule size on its trajectory for $Re = 20$, $q = 0.56$, $Ca = 0.1$: (a) $a/R = 0.4$, (b) $a/R = 0.2$. The streamline legend is the same as in Figure 10.

which can be quantified by means of the stored elastic energy $E(t)$, given by

$$E(t) = \int_{A_0} W^{SK}(\lambda_1, \lambda_2, t) dA_0, \qquad (5.1)$$

where W^{SK} is given by equation (2.1) and A_0 is the initial surface area of the capsule. When the capsule is in the bifurcation region, the maximum of the stored elastic energy, normalized by $a^2 G_s$, drops from 0.91 to 0.2 when the size of the capsule decreases from $0.4R$ to $0.2R$. This means that the smaller capsule is less deformed than the larger one. This is due to the fact that the shear rate varies across the tube and that the effective capillary number to which the capsule is subjected is then $Ca \times a/R$, rather than just Ca. As the smaller capsule is less deformed, its centre does not deviate much from the the centre streamline: the capsule follows it into the straight tube in this case ($q = 0.56$). The larger capsule, however, deviates from the centre streamline and is attracted into the side branch. We find that the background flow also plays an important role in path selection of capsules with different sizes, as it will be discussed in Section 6.1.

5.3. *Path selection phase diagram*

A simple way to characterize path selection of a capsule is to define the critical branch flow ratio q_c, above which the capsule enters the side branch: the capsule thus flows in the straight tube if $q < q_c$, and in the side branch otherwise. For given values of Re and Ca, we progressively increase q from 0.1 by large steps $\Delta q = 0.05$ until we find the transition, where the capsule flows into the side branch rather than the straight tube. We then refine the step to $\Delta q = 0.02$ around the transition region. The value of q_c is taken as the average of the two successive branch flow ratios q wherein the capsule enters the side branch for the largest or remains in the main tube for the smallest. Therefore q_c is determined within ± 0.01. Near the transition, we have conducted tests using finer grid resolutions ($\Delta x = \Delta y = \Delta z = 0.031R$) and found that the trajectories of the capsule remain unchanged.

The critical branch flow ratio is shown in Figure 12 as a function of the flow Reynolds number for capsules with different sizes and membrane shear elasticity. In the extreme case of an infinitely small capsule (i.e. $a/R = 0$), the capsule follows the unperturbed streamline. For low inertia ($Re = 0.25$), $q_c = 0.48 \sim 0.49$, which means that the capsule tends to favor the side branch when the flow split is even. This is what we observe for $Ca/Re = 0.005$ or 0.02, where the capsule is only slightly deformed and behaves as a
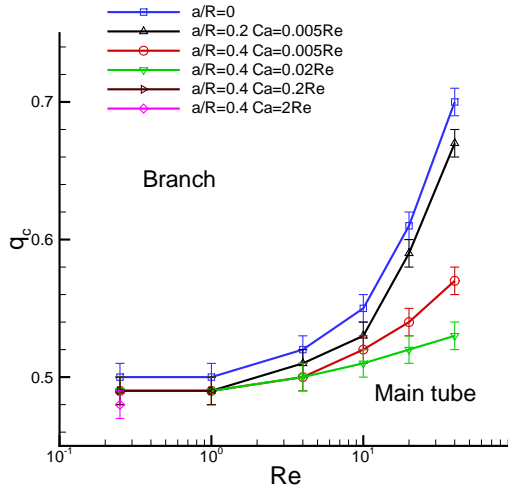
FIGURE 12. Phase diagram: critical branch flow ratio as a function of the tube Reynolds number for capsules with different sizes and membrane shear elasticity. For $q > q_c$, the capsule flows into the side branch.

solid sphere ($Ca = 0.0013$ or 0.005). Interestingly, this still occurs in the case $Ca/Re = 2$ ($Ca = 0.5$ - pink diamond in Figure 12), even though the capsule is quite deformed under these conditions as can be surmised from Figure 7. This is consistent with the two-dimensional simulation by Woolfenden & Blyth (2011) in Stokes flow. For $Re > 1$, q_c increases significantly when Re increases and the capsule size ratio decreases. Up to $Re \leqslant 4$, the main effect on q_c is only due to size ratio and thus to confinement of the capsule by the tube. The influence of capsule deformability becomes significant at larger flow rates corresponding to $Re \geqslant 10$.

6. Discussion and conclusion

We have studied the three-dimensional flow of an initially spherical capsule through a straight tube with a right-angled side branch, using an immersed boundary lattice Boltzmann method. This flow configuration is interesting as it leads to non-symmetric flow conditions between the two branches, contrary to the classical T-junction that is equivalent in terms of geometry and has received great attention. The study allows to elucidate the effects of flow split ratio, flow strength and capsule size ratio ($a/R \leqslant 0.4$) on the capsule path selection at the bifurcation. It also provides us with information on the capsule deformation and corresponding stress level in the membrane.

The path selection results are well summarized by means of the critical branch flow ratio q_c, which is the lower bound of the flow split ratio q, for which the capsule enters the side branch. For low Reynolds numbers, the critical branch flow ratio is very slightly below 0.5, which means that the capsule favors the side branch at equal flow split, but otherwise takes a path which is essentially determined by the value of q. This result is qualitatively consistent with the earlier numerical study of Woolfenden & Blyth (2011). However the authors used a two-dimensional model and a simple generalized Hooke's law for the membrane, which renders impossible any quantitative comparison.

We also consider flows with significant inertial effects, which had not been studied before. Such flows are encountered in fast flowing microfluidic devices (Di Carlo *et al.*
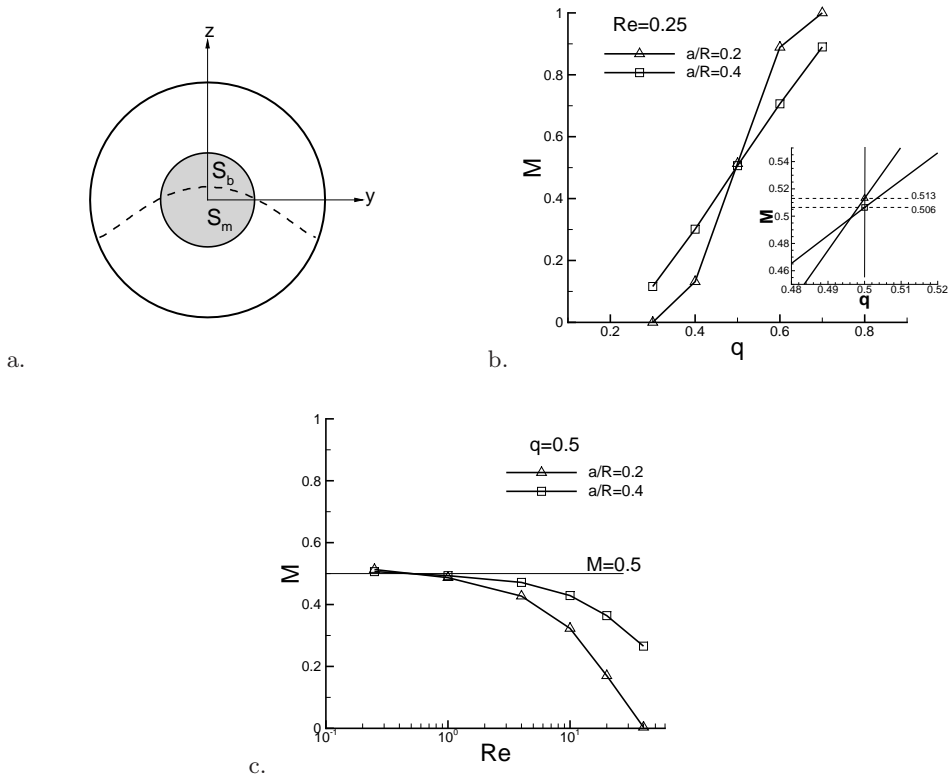
FIGURE 13. (a) Illustration for the definition of the momentum ratio. The dash line is a fluid separation line (for $q = 0.5$, $Re = 20$), which divides the cross-sectional area of the capsule (shaded circle) into two regions (S_b and S_m) covered by fluid elements that finally enter the side branch and downstream main tube, respectively. Momentum ratios of capsules with $a/R = 0.2$ and 0.4 as a function of (b) q at $Re = 0.25$, (c) Re at $q = 0.5$.

2007) or when millimetric capsules flow in fairly large capillary tubes. We find that the critical branch flow ratio is then larger than 0.5 and increases significantly with the Reynolds number, when $Re \geqslant 10$. However, q_c tends to decrease when the capsule size and/or deformation increase. This indicates that at equal flow split, the capsule tends to flow straight in the main tube when inertial effects are significant. This is a consequence of the effects of inertia on the background flow in the branched tube, which alters the shape of the fluid separation line in the upstream cross-section S_c, as discussed in details in the following Section 6.1.

6.1. *Background flow momentum split: a simple model of path selection*

All the above results have been obtained with the full fluid-structure-interaction model, which is quite intricate and necessitates long computations. It is of interest to consider a much simpler model, based on the interaction of the background flow with the undeformed capsule, and investigate the validity limits of this model by comparing the predictions to the ones provided by the full model.

In this simple model, we assume that the presence of the capsule does not change the background flow significantly, and evaluate the interaction between the undeformed capsule and the unperturbed flow in section S_c. The model is based on the ascertainment

that the cross-sectional area of the capsule (the shadowed area in Figure 13a) in the plane S_c is divided by the fluid separation line (section 4) into two distinct regions, S_b and S_m, having fluid elements that, respectively, enter the side branch and the downstream main tube eventually (Figure 13a). We then define the ratio M between the momentum of the fluid elements in S_b and the total momentum of fluid elements in the cross-sectional area of the capsule $S_b + S_m$:

$$M = \frac{\int_{S_b} \rho u(y, z) dS_b}{\int_{S_b} \rho u(y, z) dS_b + \int_{S_m} \rho u(y, z) dS_m}, \qquad (6.1)$$

where $u(y, z)$ is the fluid velocity along the x-direction in S_c. We then assume that for $M > 0.5$, the capsule enters the side branch. The evolution of M with flow split q at low Re is shown in Figure 13b, while the effect of Re on M at equal flow split $q = 0.5$ is shown in Figure 13c.

At equal flow split $q = 0.5$ and for low Reynolds number ($Re = 0.25$), M is slightly larger than 0.5 for both capsules (see insert of Figure 13b), suggesting that the slight momentum unbalance of the background flow helps send the capsule into the side branch. This is consistent with the predictions of the phase diagram, wherein q_c is below 0.5 for both capsules. Similarly, for $q > 0.5$ (resp. $q < 0.5$), the momentum is $M > 0.5$ (resp. $M < 0.5$) and the capsule flows into the side (resp. main) branch. This corresponds to the full model results shown in Figure 6. For $q = 0.5$, an increase of Re leads to a decrease of M: this means that the background flow tends to push the capsule into the main branch (Figure 13c), as predicted by the phase diagram. A qualitatively similar effect is also found with the full model, as shown in Figure 10. Note that the evolution of M with either q or Re is qualitatively the same for the two size ratios. In Figure 13c, it is seen that when $Re \geqslant 1$, the momentum ratio for a larger capsule is higher than that of a smaller capsule. This is one of the phenomena that predominantly accounts for the fact that, at the same flow split, a larger capsule enters the side branch, while a smaller one chooses the downstream main tube, as seen in Figure 11.

In order to quantify precisely the predictive power of the background flow momentum ratio on the path selection of a capsule, we define a critical branch flow ratio q_{cm}, that corresponds to $M = 0.5$. The value of q_{cm} is then computed as the average of the two successive branch flow ratios between which the value of M crosses 0.5. It is determined within ± 0.01. The values of q_{cm} for capsules with $a/R = 0.2$ and 0.4, $Ca/Re = 0.005$ or 0.02 are shown in Figure 14 and are compared with the values of q_c obtained from the full fluid-structure-interaction simulations with the capsule. For small capsules ($a/R \leqslant 0.2$) or low inertia ($Re \leqslant 4$), the values of q_c and q_{cm} are almost equal within the determination error. This indicates that the simple model, based on the momentum ratio of the undeformed capsule, is then sufficient to determine the path selection of the capsule. While this is to be expected for small capsules, it is interesting that this is also true for relatively large ones with $a/R = 0.4$. However, in this case, the values of q_c and q_{cm} begin to diverge significantly for $Re \geqslant 10$. One reason for the divergence is that the deviation of the capsule trajectory from the background flow (migration across streamlines) is mainly a result of the capsule deformability. In Figure 14, the more deformable capsule (inverted triangles with solid line) deviates more than the stiffer capsule (circles with solid line) from the background flow results (circles with dash line). This can be seen from Figure 15, where the capsule membrane shear elasticity leads to different flow trajectories under the same background flow condition. This means that the simple model can no longer be used to accurately compute the capsule path when the capsule deformation is more significant. For example, the case shown in Figure 11a, corresponds to $q = 0.56$ and
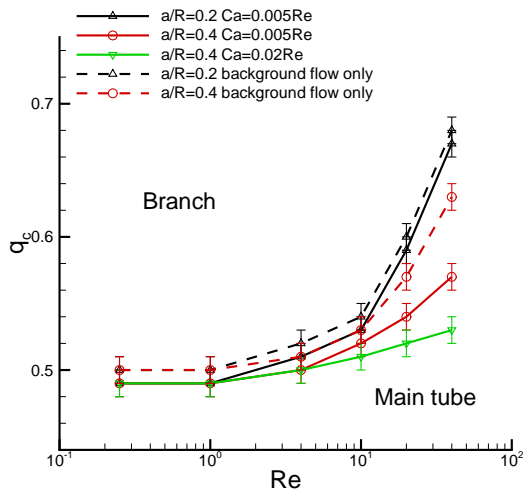
FIGURE 14. Phase diagram: critical branch flow ratio as a function of the tube Reynolds number for capsules with $a/R = 0.2$ and 0.4, $Ca/Re = 0.005$. Solid lines: full fluid-structure simulations with a capsule (see Figure 12); dash lines: q_{cm} from the background flow only.
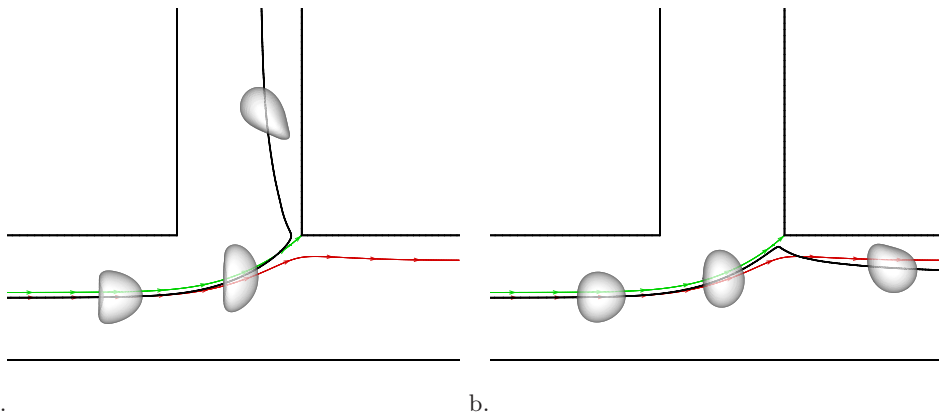

a.

b.

FIGURE 15. Effect of membrane shear elasticity on the capsule trajectory for $Re = 20$, $q = 0.53$, $a/R = 0.4$: (a) $Ca = 0.4$, (b) $Ca = 0.1$. The streamline legend is the same as in Figure 10.

$Re = 20$. According to the value $q_{cm} = 0.57$, the capsule should flow straight in the main tube, whereas it goes into the branch: this means that the simple model fails and cannot predict properly the path selection of deformed capsules. The present results therefore suggest that, when the capsule deformation is not significant ($Ca \leqslant 0.05$), the momentum ratio obtained from the background flow can be used to predict the path selection of a capsule with a reasonable accuracy. However, for large capsules undergoing significant deformation, the full fluid-structure model is compulsory to predict the capsule path.

6.2. *Limits on the parameter values*

The question which arises at this point is the range of parameters that can be achieved with typical artificial capsules. The smallest value of G_s, which has been found for stable artificial capsules with a thin albumin polymerized membrane ranges between 0.05 and 0.1 N/m for $a \sim 50$ μm (Lefebvre *et al.* 2008; Chu *et al.* 2011; de Loubens *et al.* 2014;

Gubspun *et al.* 2016). The membrane rigidity increases with the radius and becomes of the order $G_s = 0.5 \sim 1$ N/m for capsules ($a \sim 100 - 200$ μm) with a polymerized albumin or nylon membrane (Koleva & Rehage 2012; de Loubens *et al.* 2014; Gubspun *et al.* 2016). Millimetric capsules ($a \sim 1-2$ mm) with a membrane made of alginate have an elastic modulus $G_s \sim 1 - 3$ N/m (Carin *et al.* 2003; Zhang & Salsac 2012). Note that the above values of G_s correspond to minimum values, and that it is usually possible to decrease the capsule deformability (increase G_s) by increasing either the degree of polymerization, thickness of the membrane or size of the capsule. For example, to our knowledge, there are no stable millimetric capsules with G_s less than ~ 1 N/m. In order to get a significant deformation of the capsule, Ca must be large enough (typically $Ca \geqslant 0.1$ for some deformation to occur). The capsule otherwise behaves like a solid sphere.

An important experimental constraint is that the pressure drop in the system must be manageable. A rough estimate (ignoring the complex bifurcation geometry) of the pressure drop gradient $\Delta P/L$ in the branched tube is given by Poiseuille law

$$\frac{\Delta P}{L} = \frac{8\mu V}{R^2} = \frac{8 Ca G_s}{R^2}. \tag{6.2}$$

The typical length scale L of a microfluidic device is $L \sim 2$ cm. It is reasonable to limit the pressure drop to a maximum value ΔP_{max} (typically $\Delta P_{max} \sim 2 \times 10^5$ Pa.). It follows that the lower limit on the tube radius is given by

$$R_{min} = \sqrt{\frac{8 Ca G_s L}{\Delta P_{max}}}. \tag{6.3}$$

For given values of Ca and G_s, the constraint (6.3) allows us to determine a minimum value of the tube radius R (and thus of the capsule radius a, since $a = 0.2R$ or $0.4R$ in the present simulations) and check whether it is consistent with the range of size corresponding to the value of G_s (see above paragraph). The next step consists in taking a tube of radius $R \geqslant R_{min}$, a given ratio Ca/Re and compute the corresponding fluid viscosity μ and mean flow velocity V for different values of Re. It follows that within the constraint of $\Delta P_{max} \sim 2 \times 10^5$ Pa, it is very difficult to achieve high values of Re within a microtube (i.e. $R \sim 100$ μm). For example, with $Ca/Re = 0.005$, if we take $R = 100$ μm, $L = 2$ cm and $a/R = 0.4$, a reasonable value of G_s is around 0.1 N/m. The pressure constraint $\Delta P_{max} = 2 \times 10^5$ Pa leads to a maximum value $Ca = 0.125$, which corresponds to $Re = 25$ for this Ca/Re ratio. From equation 2.10, one notices that such experimental conditions can be achieved for a fluid with a density $\rho = 1000$ kg m^{-3} and a viscosity $\mu = 0.01$ Pa s. At $Re = 25$, the average fluid velocity in the tube will be 1.25 m/s. The high velocity introduces a significant challenge for capsule imaging when it is flowing in the tube. However, it also means that the device can have a high throughput. Note that the case $Re = 40$ is difficult to obtain experimentally. We have, nevertheless, used it in this paper for illustration purposes, as it shows clearly the combined effects of significant flow inertia and large capsule deformation.

6.3. *Capsule sorting*

The present results suggest that the trajectory of a capsule in a branched tube can be controlled by adjusting a range of parameters, among which are the capsule size, tube flow rate and branch flow ratio. One potential application of the results is to guide the development of microfluidic devices with a bifurcation, to separate capsules from a suspension or to sort capsules according to size and/or membrane elasticity. The present T-branch geometry with non-symmetric flow condition can be used to sort capsules according to size (the small ones in the side branch) by flowing the suspension at a

high enough rate where inertia becomes important (see Figure 11). Sorting equal size capsules according to membrane elasticity can also be achieved at high flow rates, but is trickier to achieve, since the difference in q_c values is small (see the difference between the curves corresponding to $Ca = 0.02Re$ and $Ca = 0.005Re$ in Figure 12). Another aspect to keep in mind is that it may be difficult to operate such devices under steady flow rates with a precise flow split. Furthermore, special attention should be paid to the stress level in the membrane, when the capsule is close to the bifurcation, in order to avoid damage. It is worth pointing out that the present results are obtained for tube flows generated by flow-rate control systems. Pressure-control systems such as present in the microcirculation may work in a different way. Finally, a limitation of the present work is that we have only considered a single capsule, corresponding to the infinite-dilute limit. In future studies we shall investigate capsule suspensions to establish the effect of capsule interaction.

REFERENCES

BARBER, J. O., ALBERDING, J. P., RESTREPO, J. M. & SECOMB, T. W. 2008 Simulated two-dimensional red blood cell motion, deformation, and partitioning in microvessel bifurcations. *Ann. Biomed. Engng.* **36** (10), 1690–1698.

BARBER, J. O., RESTREPO, J. M. & SECOMB, T. W. 2011 Simulated red blood cell motion in microvessel bifurcations: Effects of cell–cell interactions on cell partitioning. *Cardiovasc. Engng. Technol.* **2** (4), 349–360.

BARTHÈS-BIESEL, D. 2016 Motion and deformation of elastic capsules and vesicles in flow. *Annu. Rev. Fluid Mech.* **48**, 25–52.

BARTHÈS-BIESEL, D., DIAZ, A. & DHENIN, E. 2002 Effect of constitutive laws for two-dimensional membranes on flow-induced capsule deformation. *J. Fluid Mech.* **460**, 211–222.

BHUJBAL, S. V., DE VOS, P. & NICLOU, S. P. 2014 Drug and cell encapsulation: alternative delivery options for the treatment of malignant brain tumors. *Adv. drug Deliv. Rev.* **67-68**, 142–153.

BOUZIDI, M., FIRDAOUSS, M. & LALLEMAND, P. 2001 Momentum transfer of a boltzmann-lattice fluid with boundaries. *Phys. Fluids* **13** (11), 3452–3459.

CARIN, M.L, BARTHÈS-BIESEL, D., EDWARDS-LÉVY, F., POSTEL, C. & ANDREI, D. C. 2003 Compression of biocompatible liquid-filled hsa-alginate capsules: Determination of the membrane mechanical properties. *Biotechnol. Bioeng.* **82** (2), 207–212.

CARR, R. T. & KOTHA, S. L. 1995 Separation surfaces for laminar flow in branching tubes—effect of reynolds number and geometry. *J. Biomech. Engng* **117**, 442–447.

CHARRIER, J. M., SHRIVASTAVA, S. & WU, R. 1989 Free and constrained inflation of elastic membranes in relation to thermoforming—non-axisymmetric problems. *J. Strain Anal.* **24**, 55–74.

CHIEN, S., TVETENSTRAND, C. D., EPSTEIN, M. A. & SCHMID-SCHONBEIN, G. W. 1985 Model studies on distributions of blood cells at microvascular bifurcations. *Am. J. Physiol. Heart Circ. Physiol.* **248** (4), H568–H576.

CHU, T. X., SALSAC, A.-V., LECLERC, E., BARTHÈS-BIESEL, D., WURTZ, H. & EDWARDS-LÉVY, F. 2011 Comparison between measurements of elasticity and free amino group content of ovalbumin microcapsule membranes: Discrimination of the cross–linking degree. *J. Colloid Interf. Sci.* **355**, 81 – 88.

CORDASCO, D. & BAGCHI, P. 2013 Orbital drift of capsules and red blood cells in shear flow. *Phys. Fluids* **25** (9), 091902.

DABADE, V., MARATH, N. K. & SUBRAMANIAN, G. 2016 The effect of inertia on the orientation dynamics of anisotropic particles in simple shear flow. *J. Fluid Mech.* **791**, 631–703.

DE LOUBENS, C., DESCHAMPS, J., GEORGELIN, M., CHARRIER, A., EDWARD-LÉVY, F. & LEONETTI, M. 2014 Mechanical characterization of cross–linked serum albumin microcapsules. *Soft Matter* **10**, 4561 – 4568.

DI CARLO, D., IRIMIA, D., TOMPKINS, R. G. & TONER, M. 2007 Continuous inertial focusing, ordering, and separation of particles in microchannels. *Proc. Natl. Acad. Sci. U.S.A.* **104** (48), 18892–18897.

DODDI, S. K. & BAGCHI, P. 2008 Lateral migration of a capsule in a plane poiseuille flow in a channel. *Intl J. Multiphase Flow* **34** (10), 966–986.

DOYEUX, V., PODGORSKI, T., PEPONAS, S., ISMAIL, M. & COUPIER, G. 2011 Spheres in the vicinity of a bifurcation: elucidating the zweifach–fung effect. *J. Fluid Mech.* **674**, 359–388.

DUPONT, C., SALSAC, A.-V., BARTHÈS-BIESEL, D., VIDRASCU, M. & LE TALLEC, P. 2015 Influence of bending resistance on the dynamics of a spherical capsule in shear flow. *Phys. Fluids* **27**, 051902.

ENDEN, G. & POPEL, A. S. 1992 A numerical study of the shape of the surface separating flow into branches in microvascular bifurcations. *J. Biomech. Engng* **114**, 398–405.

ENDEN, G. & POPEL, A. S. 1994 A numerical study of plasma skimming in small vascular bifurcations. *J. Biomech. Engng* **116**, 79–88.

FÅHRAEUS, R. 1929 The suspension stability of the blood. *Physiol. Rev.* **9**, 241–274.

FENTON, B. M., CARR, R. T. & COKELET, G. R. 1985 Nonuniform red cell distribution in 20 to 100 μm bifurcations. *Microvasc. Res.* **29**, 103–126.

FUNG, Y. C. 1973 Stochastic flow in capillary blood vessels. *Microvasc. Res.* **5**, 34–48.

GREEN, A. E. & ADKINS, J. E. 1960 *Large Elastic Deformations*. Oxford: Oxford University Press.

GUBSPUN, J., GIRES, P.-Y., DE LOUBENS, C., BARTHÈS-BIESEL, D., DESCHAMPS, J., GEORGELIN, M., LÉONETTI, M., LECLERC, E., EDWARDS-LÉVY, F. & SALSAC, A.-V. 2016 Size and concentration effect on the mechanical properties of cross-linked albumin capsule membranes. *Colloid and Polymer Science* **In Press**.

GUO, Z.-L., ZHENG, C.-G. & SHI, B.-C. 2002*a* Discrete lattice effects on the forcing term in the lattice boltzmann method. *Phys. Rev. E* **65**, 046308.

GUO, Z.-L., ZHENG, C.-G. & SHI, B.-C. 2002*b* Non-equilibrium extrapolation method for velocity and pressure boundary conditions in the lattice boltzmann method. *Chin. Phys.* **11**, 366.

HELMY, A. & BARTHÈS-BIESEL, D. 1982 Migration of a spherical capsule freely suspended in an unbounded parabolic flow. *J. Méc. Théor Appl.* **1** (5), 859–880.

HU, X.-Q., SALSAC, A.-V. & BARTHÈS-BIESEL, D. 2012 Flow of a spherical capsule in a pore with circular or square cross-section. *J. Fluid Mech.* **705**, 176–194.

KOLEVA, I. & REHAGE, H. 2012 Deformation and orientation dynamics of polysiloxane microcapsules in linear shear flow. *Soft Matter* **8**, 3681 – 3693.

LEFEBVRE, YANNICK, LECLERC, E., BARTHÈS-BIESEL, D., WALTER, J. & EDWARDS-LÉVY, F. 2008 Flow of artificial microcapsules in microfluidic channels: a method for determining the elastic properties of the membrane. *Phys. Fluids* **20**, 123102–1–123102–10.

MASAELI, M., SOLLIER, E., AMINI, H., MAO, W., CAMACHO, K., DOSHI, N.T, MITRAGOTRI, S., ALEXEEV, A. & DI CARLO, D. 2012 Continuous inertial focusing and separation of particles by shape. *Phys. Rev. X* **2** (3), 031017.

PESKIN, C. S. 1977 Numerical analysis of blood flow in the heart. *J. Comput. Phys.* **25** (3), 220–252.

POPEL, A. S. & JOHNSON, P. C. 2005 Microcirculation and hemorheology. *Annu. Rev. Fluid Mech.* **37**, 43.

POZRIKIDIS, C. 2005*a* Axisymmetric motion of a file of red blood cells through capillaries. *Phys. Fluids* **17** (3), 031503.

POZRIKIDIS, C. 2005*b* Numerical simulation of cell motion in tube flow. *Ann. Biomed. Engng* **33** (2), 165–178.

PRIES, A. R., SECOMB, T. W. & GAEHTGENS, P. 1996 Biophysical aspects of blood flow in the microvasculature. *Microvasc. Res.* **32**, 654–667.

RACHIK, M., BARTHÈS-BIESEL, D., CARIN, M.l & EDWARDS-LÉVY, F. 2006 Identification of the elastic properties of an artificial capsule membrane with the compression test: effect of thickness. *J. Colloid Interface Sci.* **301** (1), 217–226.

RAMANUJAN, S. & POZRIKIDIS, C. 1998 Deformation of liquid capsules enclosed by elastic membranes in simple shear flow: large deformations and the effect of fluid viscosities. *J. Fluid Mech.* **361**, 117–143.

RISSO, F. & CARIN, M. 2004 Compression of a capsule: Mechanical laws of membranes with negligible bending stiffness. *Phys. Rev. E* **69** (6), 061601.

ROBERTS, B. W. & OLBRICHT, W. L. 2006 The distribution of freely suspended particles at microfluidic bifurcations. *AIChE J.* **52**, 199–206.

RONG, F. W. & CARR, R. T. 1990 Dye studies on flow through branching tubes. *Microvasc. Res.* **39**, 186–202.

ROSÉN, T., LUNDELL, F. & AIDUN, C. K. 2014 Effect of fluid inertia on the dynamics and scaling of neutrally buoyant particles in shear flow. *J. Fluid Mech.* **738**, 563–590.

SECOMB, T. W., STYP-REKOWSKA, B. & PRIES, A. R. 2007 Two-dimensional simulation of red blood cell deformation and lateral migration in microvessels. *Ann. Biomed. Engng* **35** (5), 755–765.

SHRIVASTAVA, S. & TANG, J. 1993 Large deformation finite element analysis of non-linear viscoelastic membranes with reference to thermoforming. *J. Strain Anal.* **28**, 31–51.

SKALAK, R., TOZEREN, A., ZARDA, R. P. & CHIEN, S. 1973 Strain energy function of red blood cell membranes. *Biophys. J.* **13** (3), 245–264.

SUI, Y., CHEW, Y. T., ROY, P. & LOW, H. T. 2008a A hybrid method to study flow-induced deformation of three-dimensional capsules. *J. Comput. Phys.* **227** (12), 6351–6371.

SUI, Y., LOW, H. T., CHEW, Y. T. & ROY, P. 2008b Tank-treading, swinging, and tumbling of liquid-filled elastic capsules in shear flow. *Phys. Rev. E* **77**, 016310.

SUI, Y., TEO, C. J. & LEE, P. S. 2012 Direct numerical simulation of fluid flow and heat transfer in periodic wavy channels with rectangular cross-sections. *Int. J. Heat Mass Transf.* **55**, 73–88.

SVANES, K. & ZWEIFACH, B. W. 1968 Variations in small blood vessel hematocrits produced in hypothermic rats by micro-occlusion. *Microvasc. Res.* **1**, 210–220.

WOOLFENDEN, H. C. & BLYTH, M. G. 2011 Motion of a two-dimensional elastic capsule in a branching channel flow. *J. Fluid Mech.* **669**, 3–31.

WU, W.-Y., WEINBAUM, S. & ACRIVOS, A. 1992 Shear flow over a wall with suction and its application to particle screening. *J. Fluid Mech.* **243**, 489–518.

YAN, Z.-Y., ACRIVOS, A. & WEINBAUM, S. 1991 A three-dimensional analysis of plasma skimming at microvascular bifurcations. *Microvasc. Res.* **42**, 17–38.

YE, H., HUANG, H. & LU, X.-Y. 2015 Numerical study on dynamic sorting of a compliant capsule with a thin shell. *Comput. Fluids* **114**, 110–120.

ZHANG, L. & SALSAC, A.-V. 2012 Can sonication enhance release from liquid-core capsules with a hydrogel membrane? *J. Colloid Interf. Sci.* **368**, 648–654.

ZHONG-CAN, O.-Y. & HELFRICH, W. 1989 Bending energy of vesicle membranes: General expressions for the first, second, and third variation of the shape energy and applications to spheres and cylinders. *Phys. Rev. A* **39** (10), 5280.